F I N A L
/ N U 2 - C R
6 C / T
8 0 9 5 3

Computational Aeroacoustics and Numerical Simulation of Supersonic Jets

Final Report on NASA Grant NAG 1-1479

Philip J. Morris and Lyle N. Long
Department of Aerospace Engineering
The Pennsylvania State University

Feb. 1993 - Feb. 1996

Contents

Chapter 1

Introduction

This is the final report on NASA Grant No. NAG 1-1479 entitled, "Computational Aeroacoustics and Numerical Simulation of Supersonic Jets." The Principal Investigators are Drs. Philip J. Morris and Lyle N. Long of the Department of Aerospace Engineering at the Pennsylvania State University.

The research project has been a computational study of computational aeroacoustics algorithms and numerical simulations of the flow and noise of supersonic jets. During this study a new method for the implementation of solid wall boundary conditions for complex geometries in three dimensions has been developed. In addition, a detailed study of the simulation of the flow in and noise from supersonic circular and rectangular jets has been conducted. Extensive comparisons have been made with experimental measurements. A summary of the results of the research program are attached as the main body of this report in the form of two publications. In addition, the report lists the names of the students who were supported by this grant, their degrees, and the titles of their dissertations. In addition, a list of presentations and publications made by the Principal Investigators and the research students is also included.

Chapter 2

Publications and Presentations

Morris, P. J., Long, L. N., Chung, C. and Chyczewski, T., "Computational aeroacoustics algorithms: nonuniform grids," *AIAA Paper* 94-2295, 25th AIAA Fluid Dynamics Conference, June 1994.

Chung, C. and Morris, P. J., "Wave propagation and scattering in computational aeroacoustics," ICASE/LaRC Workshop in Benchmark Problems in Computational Aeroacoustics, Hampton, VA, October 1994.

Morris, P. J., Chung, C. and Pautet, L. R., "Acoustic scattering: a numerical simulation," 47th APS/Division of Fluid Dynamics Meeting, Atlanta, GA, November 1994.

Chung, C. and Morris, P. J., "A new boundary treatment for two- and three-dimensional acoustic scattering problems," AIAA/CEAS Aeroacoustics Conference, Munich, Germany, June 1995.

Chung, C. and Morris, P. J., "Acoustic scattering from two- and three-dimensional bodies," submitted for publication to *J. Computational Acoustics*, August 1996. (copy attached below)

Chyczewski, T. and Long, L. N., "Numerical prediction of the noise produced by a perfectly-expanded rectangular jet," 2nd AIAA/CEAS Aeroacoustics Conference, State College, PA, May 1996. (copy attached below)

Chapter 3

Graduate Student Researchers

Tom Chyczewski, "A time-dependent, three-dimensional numerical study of supersonic rectangular jet flow and noise using the full Navier-Stokes equations," **Ph. D.** thesis, Aerospace Engineering, 1996. Present Occupation: Research Engineer at Allison Gas Turbines, Indianapolis, IN.

Cathy Chung, "Wave propagation and scattering in computational aeroacoustics," **Ph.D.** thesis, Aerospace Engineering, 1995. Present Occupation: Homemaker and mother.

Chapter 4

Appendix: Summary Papers

ACOUSTIC SCATTERING FROM
TWO- AND THREE-DIMENSIONAL BODIES

CATHY CHUNG and PHILIP J. MORRIS

Department of Aerospace Engineering, Pennsylvania State University
233P Hammond Building, University Park, PA, 16802, USA

In this paper we consider the scattering of sound by two- and three-dimensional bodies with arbitrary geometries. Particular emphasis is placed on the methodology for the implementation of solid wall boundary conditions for high-order, high-bandwidth numerical schemes. The Impedance Mismatch Method (IMM) is introduced to treat solid wall boundaries. In this method the solid wall is simulated using a wall region in which the characteristic impedance is set to a different value from that in the fluid region. This method has many advantages over traditional solid wall boundary treatments, including simplicity of coding, speed of computation and the ability to treat curved boundaries. This method has been used to solve a number of acoustic scattering problems to demonstrate its effectiveness. These problems include acoustic reflections from an infinite plate, acoustic scattering from a two-dimensional finite plate and a cylinder, and acoustic scattering by a sphere and a cylindrical shell.

1. Introduction

Acoustic scattering by solid bodies is of importance in engineering noise prediction and control. In order to simulate acoustic scattering accurately, we need high-order numerical schemes as well as methods to implement solid wall boundary conditions for such high-order schemes. In recent years, a number of high-order schemes have been developed. One of them is the Dispersion-Relation-Preserving (DRP) scheme developed by Tam and Webb [7]. This scheme is used in this paper.

The most important consideration in computations of acoustic scattering by solid bodies is the implementation of solid wall boundary conditions. For inviscid flow the solid wall boundary condition requires that the velocity normal to the wall is zero. For low-order finite difference schemes or finite volume schemes, the imposition of solid wall boundary conditions can usually be carried out in a straightforward manner (Khan et al [3], Huh et al [2]);Though, it should be noted that in these references, the problem was reformulated to solve for the scattered field only. For high-order finite difference schemes, treatment of the wall condition is complicated and it has had little investigation. Recently, Tam and Dong [6] proposed a way to implement solid wall boundary conditions for high-order finite difference DRP schemes. In their method, ghost points are needed and the seven-point central difference spatial stencil

must be changed to a one-sided stencil when computations are performed at grid points within three rows of the solid surface. For an object with a simple geometry, such as a flat plate, this solid wall boundary condition can be used relatively easily. But for a complicated surface where the boundary is curved, the implementation of this wall boundary condition involves considerable work in coding and long computer times. This is especially true if the calculations are to be performed on computers with parallel architecture. Kurbatskii and Tam [4] have extended the plane wall boundary method of Tam and Dong [6] to two-dimensional curved walls.

In this paper we introduce a very efficient method to implement solid wall boundary conditions. This is the Impedance Mismatch Method (IMM). This method can be applied easily to high-order finite difference schemes. In this method the solid wall is simulated using a wall region in which the characteristic impedance is set to a different value from that in the fluid region. When acoustic waves encounter the interface between the two different regions, they will be reflected in-phase; the interface acts just like a solid surface. Actually, in this method, no wall boundary conditions need to be implemented, all that is needed is to define a body region and to set a different characteristic impedance in this region. Since this method does not involve any changes in the stencil, it can be used to represent the geometry of any object without difficulty. Also it makes the computation much faster and coding much simpler compared to traditional ways of dealing with solid wall boundaries.

In the next section of this paper, the one-dimensional linearized Euler equations are used to introduce the Impedance Mismatch Method. Then several numerical simulations are performed for acoustic scattering by two-dimensional bodies, including acoustic reflection from an infinite plate, and acoustic scattering from a finite plate and from a cylinder. Following that, acoustic scattering by three-dimensional bodies is computed. Examples include acoustic scattering by a sphere and a cylindrical shell. The numerical results are compared with either analytical solutions or solutions obtained using traditional solid wall boundary conditions. Finally, the advantages and some disadvantages of the IMM are given.

2. The Impedance Mismatch Method (IMM)

In this section a one-dimensional example is used to fix the idea of the IMM. First, the elementary problem of plane wave reflections is presented to introduce the characteristic impedance. However, it is found that when a direct simulation of this problem is extended to two dimensions a numerical instability occurs. In order to overcome this difficulty, an auxiliary problem is proposed. Analysis shows that the auxiliary problem gives the same solution as the physical problem in the region of interest external to the body.

2.1. *The Physical Problem*

From classical acoustics theory, it is known that when a plane wave in a fluid medium impinges normally to the boundary of a contiguous second medium, a reflected wave is generated in the first medium and a transmitted wave moves into the second medium. The ratio of the pressure amplitude of the reflected wave to that of incident wave depends on

the characteristic impedances, ρa, of the two media. the pressure amplitude ratio is given by

$$|p_r/p_i| = \frac{\rho_2 a_2 - \rho_1 a_1}{\rho_2 a_2 + \rho_1 a_1} \qquad (2.1)$$

where p_i, p_r are the incident and reflected pressures respectively; ρ_1 and ρ_2 are the mean densities in the first and second media respectively, and a_1 and a_2 are respective speeds of sound. This relation is obtained using the conditions that the pressure and the particle velocity are continuous at the boundary between the two media. This means that the normal derivatives of the pressure and the particle velocity are discontinuous. When the second medium has a much higher characteristic impedance, most of the wave energy is reflected. As the ratio of the characteristic impedance of the second medium to the first approaches infinity, all the incident waves are reflected. The second medium acts like a solid object. Thus, setting a higher impedance in a certain region can be used to simulate the effect of a solid object in this region. This is the basic idea behind the IMM. In the present formulation the speed of sound inside and outside the body is kept the same. This means that the wave speed is constant throughout the domain and permits the CFL number to be kept at almost the same value as when no object is present. Thus, it is the mean density in the wall region that is modified to provide the impedance mismatch.

This problem is governed by the linearized Euler equations. The one-dimensional form of these equations without mean flow is

$$\frac{\partial \rho}{\partial t} + \rho_0 \frac{\partial u}{\partial x} = 0 \qquad (2.2)$$

$$\frac{\partial u}{\partial t} + \frac{1}{\rho_0} \frac{\partial p}{\partial x} = 0 \qquad (2.3)$$

$$\frac{\partial p}{\partial t} + \rho_0 a_0^2 \frac{\partial u}{\partial x} = 0 \qquad (2.4)$$

In above equations, all quantities are nondimensionalized by characteristic scales: the mesh size of the numerical simulation ($\Delta x = \Delta y$) for a length scale; the ambient speed of sound (a_{amb}) for a velocity scale; the ambient density (ρ_{amb}) for a density scale; $\rho_{amb} a_{amb}^2$ for a pressure scale. ρ_0 is the nondimensionalized mean density and a_0 is the nondimensionalized local mean sound speed. a_0 is equal to unity at all points for a constant speed of sound and ρ_0 is equal to unity exterior to the body.

An initial value problem is now solved to test the IMM. The computational domain is $-100 \leq x \leq 100$. The wall region is $50 \leq x \leq 100$, inside which the mean density, $\rho_2 = 30$. An acoustic pulse is generated in the center of the domain at $t = 0$. The initial conditions are

$$p = \rho = \exp(-\frac{\ln 2}{25} x^2), \ u = 0 \qquad (2.5)$$

Figure 1 shows the computed pressure distribution at $t = 75, \Delta t = 0.05$. The analytical solution is also plotted. The first pulse from the left-travelling disturbance from the initial pulse. The second pulse is the reflected wave from the interface at $x = 50$, also traveling to the left. The third pulse is the transmitted wave, traveling to the right inside the wall
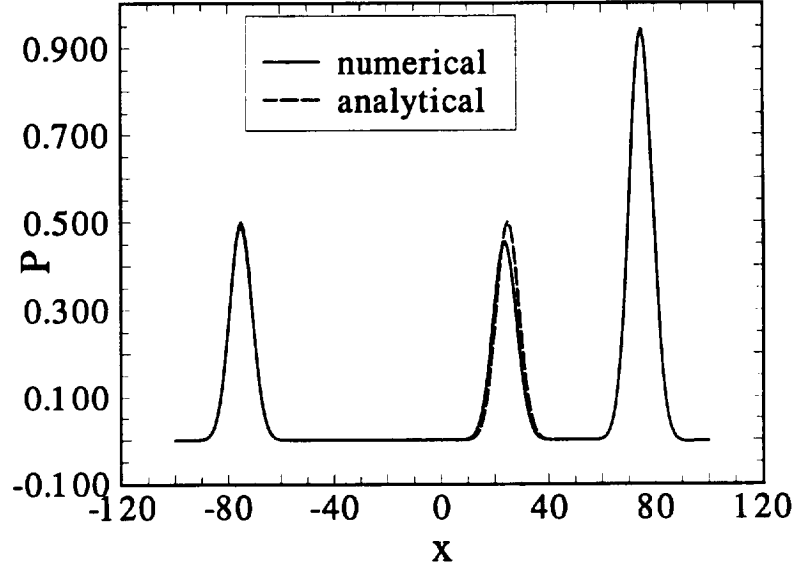
Fig. 1. Pressure at $t = 75$ for the one-dimensional physical problem.

region. It can be seen that the pressure wave has been reflected after it encounters the interface at $x = 50$. The agreement between the computed and analytical solutions is good, but some small errors can still be seen in the plot. These errors are mainly due to the finite choice of the mean density in the wall region ρ_2 and ambiguities about the exact position of the wall boundary. These issues are discussed in later sections.

The above example demonstrates that the IMM is applicable to this simple one- dimensional problem; however, when this method is used in multi-dimensional cases, instability occurs when the same time step is used. It is perhaps surprising that the one-dimensional problem gives any form of accurate solution. In Eqs. (2.3) and (2.4), the time derivatives are continuous functions. The coefficients and the spatial derivatives are only piecewise continuous and it is only in combination that they produce continuous functions. Finite-difference approximations depend on the smoothness of the function for accuracy. This is particularly true for high-order finite-difference approximations. Thus the finite-difference approximation to the spatial derivative will be inaccurate in the present case in the vicinity of the interface. So the large discontinuity in the coefficient (ρ_0/ρ_{amb}) will not be balanced by an accurate discontinuous behavior in the approximation to the spatial derivative. In order to overcome this problem, an auxiliary problem is introduced in which the discontinuous coefficients are combined with the primitive variables under the spatial derivative operator.

2.2. *The Auxiliary Problem*

The 1-D linearized Euler equations without mean flow are re-written as

$$\frac{\partial \rho}{\partial t} + \frac{\partial \hat{u}}{\partial x} = 0 \tag{2.6}$$

$$\frac{\partial u}{\partial t} + \frac{\partial \hat{p}}{\partial x} = 0 \tag{2.7}$$

$$\frac{\partial p}{\partial t} + \frac{\partial \hat{u}}{\partial x} = 0 \tag{2.8}$$

where $\hat{\rho} = \rho/\rho_0$, $\hat{u} = u\rho_0$, $\hat{p} = p/\rho_0$. Note that a_0 equals unity. This set of equations is the same as that in the physical problem in the fluid region and wall region, but not at the interface, since ρ_0 is only piecewise uniform and has a jump at interface. For this set of equations, the coefficients are continuous. The condition is imposed that variables $\hat{\rho}$, $\hat{u}$ and $\hat{p}$ are also continuous at the interface of the two media. This is not the physical problem or interface condition. For a normal incident plane wave, the pressure amplitude of the reflected waves is found to be

$$|\hat{p}_r/\hat{p}_i| = \frac{1/\rho_2 - 1}{1/\rho_2 + 1} \tag{2.9}$$

If the wall region still mimics a solid wall in this case, then the mean density in the wall region must be set to a lower value instead of a higher value than that in the fluid region. This assumes that the mean speed of sound is kept the same in both the fluid and the wall regions. Since ρ_0 is always unity in the fluid region, the physical solution then can be obtained in this region from the solution of this auxiliary problem.
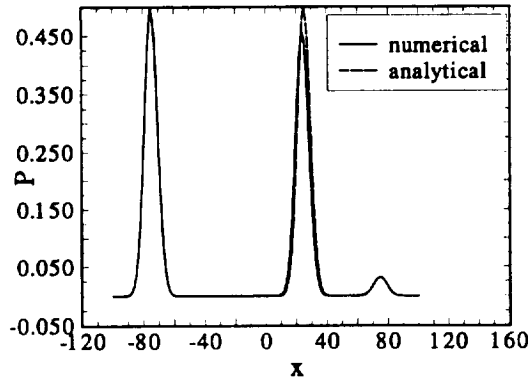

Fig. 2. Pressure at $t = 75$ for the
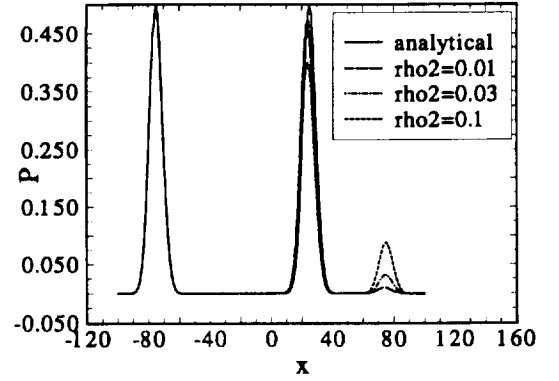one-dimensional auxiliary problem.

Fig. 3. Pressure at $t = 75$ for the
one-dimensional auxiliary problem for different
density ratios.

The same initial value problem has been solved by setting $\rho_2 = 1/30$ in the wall region. However, this time, the auxiliary problem is implemented. Figure 2 shows the computed

pressure distribution at $t = 75$. The analytical solution is also plotted. It can be seen that the physical solution is obtained in the fluid region, and the agreement between the computed and analytical solutions is good.

Figure 3 also shows the pressure distributions for different mean density ratios in the wall region. It can be seen that the accuracy of computations depends on the density ratio; the smaller the ratio, the more closely the numerical simulation follows the rigid wall solution. But, it has been found numerically that this density ratio can not be set infinitely small due to the stability considerations. This is one of the sources of inaccuracies in the IMM.

3. Governing Equations and Algorithms

In this paper the governing equations to be solved are the linearized Euler equations. For three-dimensional flows with a mean flow only in x direction, they have the form

$$\frac{\partial U}{\partial t} + \frac{\partial E}{\partial x} + \frac{\partial F}{\partial y} + \frac{\partial G}{\partial z} = H \tag{3.10}$$

where

$$U = \begin{bmatrix} \rho \\ u \\ v \\ w \\ p \end{bmatrix}, \quad E = \begin{bmatrix} M\rho + \rho_0 u \\ Mu + p/\rho_0 \\ Mv \\ Mw \\ Mp + \rho_0 u \end{bmatrix},$$

$$F = \begin{bmatrix} \rho_0 v \\ 0 \\ p/\rho_0 \\ 0 \\ \rho_0 v \end{bmatrix}, \quad G = \begin{bmatrix} \rho_0 w \\ 0 \\ 0 \\ p/\rho_0 \\ \rho_0 w \end{bmatrix},$$

M is the mean flow Mach number and H is a source term. All the quantities are non-dimensionalized as in the previous section.

The Dispersion-Relation-Preserving (DRP) method developed by Tam and Webb [7] has been used to discretize these equations. The DRP scheme is an optimized fourth-order central finite difference scheme with a seven-point stencil in space and an optimized second-order multistep scheme in time. Non-reflecting boundary conditions are needed at the outer boundaries of the computational domain. The asymptotic non-reflecting boundary conditions of Tam and Webb [7] have been used for the two-dimensional computations in this paper and they have also been extended for the three-dimensional cases. The complete description and derivation of the schemes and the non-reflecting boundary conditions are given by Chung [1].

4. Acoustic Reflection and Scattering by Two-Dimensional Bodies

In this section a number of numerical examples are given of acoustic reflection and scattering by 2-d bodies. Solutions are obtained using the IMM and are compared with

either analytical solutions or numerical solutions obtained using the solid wall boundary conditions proposed by Tam and Dong [6].

4.1. *Acoustic Reflection of A Single Initial Acoustic Pulse By An Infinite Flat Solid Wall*
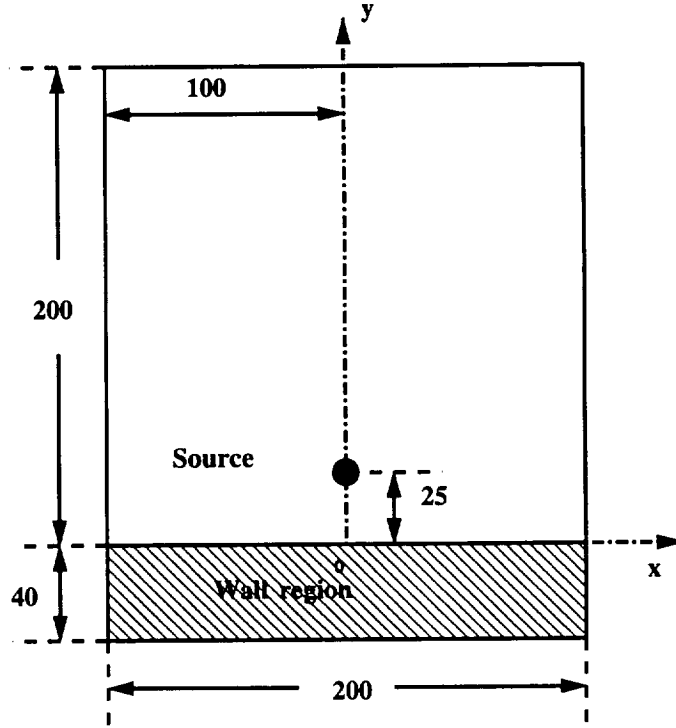

Fig. 4. Sketch of Computational Domain for Infinite Wall Reflection Problem.

First, the acoustic reflection of a two-dimensional acoustic pulse by a plane wall is considered. This is shown schematically in figure 4. The wall is located at $y = 0$. This is an initial value problem. An acoustic pulse is generated by an initial pressure disturbance with a Gaussian spatial distribution. The initial conditions are:

$$p = \rho = \exp\{-\frac{\ln 2}{25}[x^2 + (y - 25)^2]\}, \quad u = v = 0 \tag{4.11}$$

The source is placed at (0,25). The fluid domain is 201 by 201. There is uniform mean flow with Mach number 0.5 parallel to the wall. The time step, Δt is 0.05.

In order to simulate the infinite wall using the IMM, an extra wall region is needed as shown in figure 4. The thickness of this wall region is chosen to be 40. This thickness could be smaller, but in that case the source would be too close to the non-reflecting boundary of the total domain, and some wave reflections would occur at the bottom boundary. An extra wall region is needed only such wall situations at the boundary of the domain, not

for scattering by finite objects. The computations are then carried out directly. No stencil change is needed, no solid wall boundary conditions are implemented. The presence of the wall does not affect the speed of computations. Even though the extra wall region increases the amount of computations, the overall computing time is decreased compared to that using traditional solid wall boundary conditions.
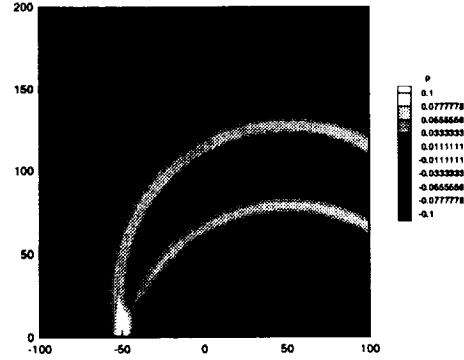

Fig. 5. Pressure Contours at $t = 100$ for Reflection of an Acoustic Pulse by an Infinite Wall With Mean Flow Mach Number $M = 0.5$.
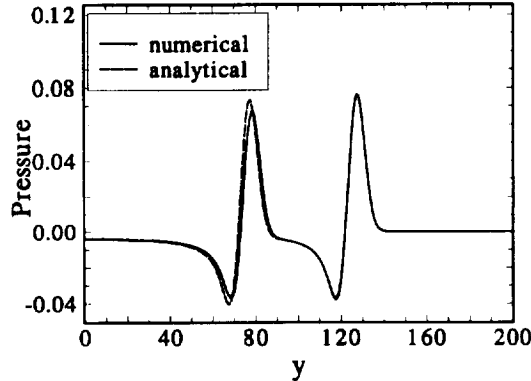

Fig. 6. Pressure distribution on y axis and $x = 50$ at time $t = 100$ for Reflection of an Acoustic Pulse by an Infinite Wall With Mean Flow Mach Number $M = 0.5$.

Figure 5 shows a calculated pressure contour associated with the acoustic pulse at $t = 100$. At this time, the pulse has reached the wall and has been reflected off the wall creating a double pulse pattern. The entire pulse has been translated downstream by the mean flow. Figure 6 shows the corresponding computed pressure waveform along the line $x = 50$, which passes the center of the pulse. The numerical result is compared with the analytical solution and the agreement is good. But some small errors can still be seen in the reflected waveform, both in its amplitude and phase. The amplitude error is mainly due to the finite choice of mean density ratio. This was discussed in section 2. The phase error is caused by the fact that the location of the wall can not be defined exactly. This is discussed further in the

following example.

4.2. *Acoustic Reflection of Time Periodic Acoustic Waves By An Infinite Flat Solid Wall*

The reflection of a periodic acoustic wave train by a solid wall is considered in the absence of a mean flow. The computational domain and the locations of the wall and the source are the same as in the previous example. The acoustic wave train is generated by a time periodic source in the energy equation. The source takes the form

$$H = 0.01 \exp\{\frac{\ln 2}{(25/8)^2}[x^2 + (y - 25)^2]\} \cos(\omega t) \tag{4.12}$$

ω is the angular frequency. 10 points per wavelength are used, so that $\omega = \pi/5$.
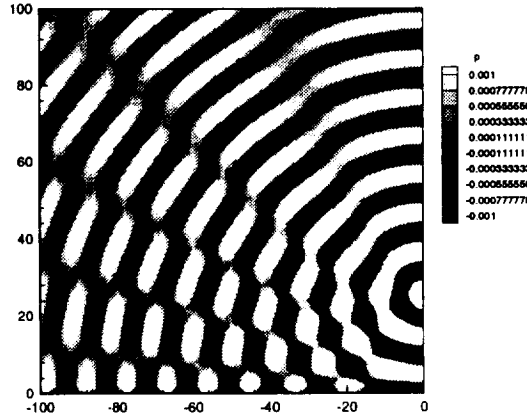

Fig. 7. Pressure Contours at $t = 180$ for Reflection of Acoustic Wave Train by Infinite Wall.

The simulation is carried out with zero initial conditions. After the transient solution has propagated out of the computational domain, the pressure fluctuation is time periodic with an angular frequency ω. Figure 7 shows the computed pressure contours adjacent to the solid wall at time $t = 180$ in the left half of the domain. The interference pattern is due to cancellation between the incident and the reflected waves. Figure 8(a) gives the corresponding pressure waveform along the y-axis. The analytical solution is also plotted. Noticeable errors can be seen in both the amplitude and the phase. In this case the wall is located at $y = 0$ in the analytical solution. Figure 8(b) also shows the pressure waveforms at the same time, but in this case the position of the wall is at $y = 0.5$ in the analytical solution. It can be seen that the agreement between the computed and analytical solutions is much better. This simulation demonstrates that there is a one grid spacing (Δy) inaccuracy in the definition of the wall position in the IMM. The mean density ratio in the IMM is specified in the following way: $\rho_0 = 1/30$ when $y \leq 0$; $\rho_0 = 1$ when $y \geq 1$, so the wall could
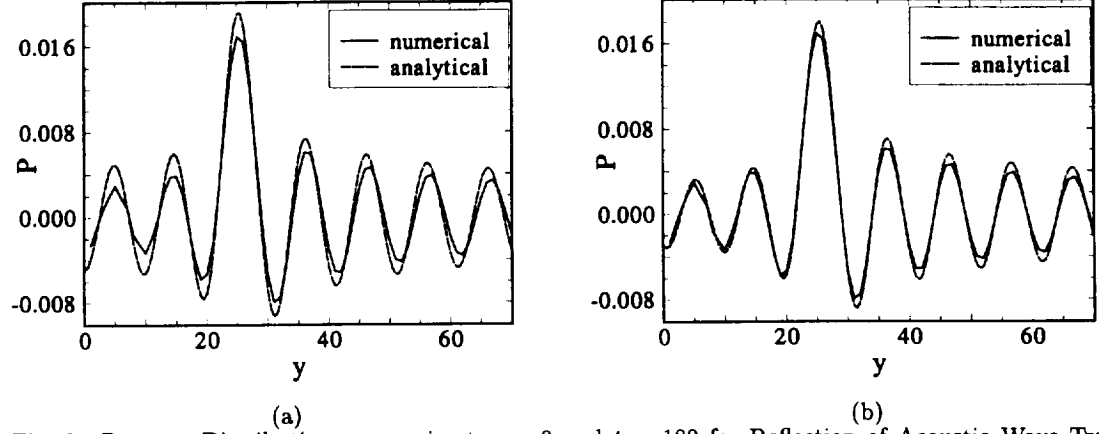
Fig. 8. Pressure Distribution on y axis at $x = 0$ and $t = 180$ for Reflection of Acoustic Wave Train by Infinite Wall. For Analytical Solutions, Wall is at (a) $y = 0.0$, (b) $y = 0.5$.

be anywhere between $y = 0$ and $y = 1$ and the numerical solution could be unchanged. This is disadvantage of the IMM. If the source is not too close to the wall, or enough grid points are used between the source and the wall, then this error is in the acceptable range. But this disadvantage can have a positive effect when curved solid boundary problems are solved using the IMM. This is shown in the following example.

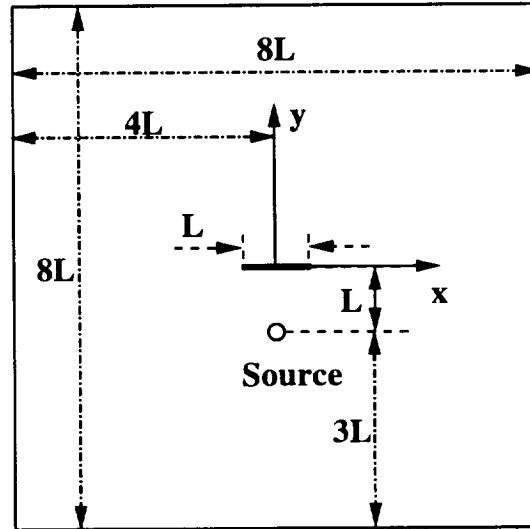### 4.3. *Acoustic Scattering of Time Periodic Acoustic Waves By A Finite Flat Plate*

Fig. 9. Sketch of Computational Domain for Finite Plate Scattering Problem

The scattering of a periodic acoustic wave train by a thin flat plate of finite length is considered as shown in figure 9. The length of the plate, $L = 25$. The domain is $8L$ by $8L$.
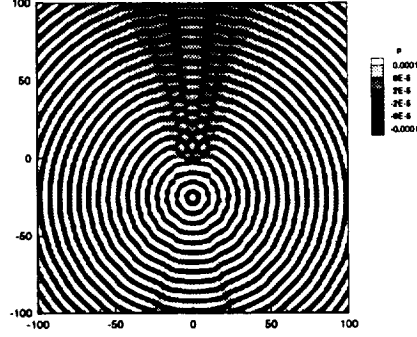
Fig. 10. Pressure Contours at $t = 194$ for Scattering of Periodic Source by a Finite Plate
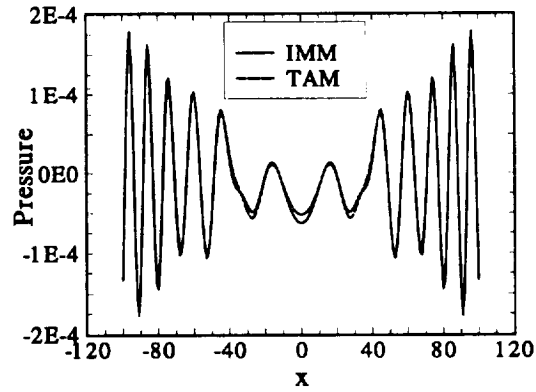

Fig. 11. Pressure Distribution Along Upper Boundary of Computational Domain for Scattering of Periodic Source by a Finite Plate

The plate is located at the center of the computational domain. The acoustic waves are generated by a simple harmonic source located at a distance of L from the middle point of the plate. The source term is incorporated into the energy equation and has the form

$$H = 0.01 \exp\{-\frac{\ln 2}{(L/8)^2}[x^2 + (y - 25)^2]\} \cos(\omega t) \tag{4.13}$$

In this numerical simulation, $L = 4\lambda$, so $\omega = 2\pi/\lambda = 0.32\pi$. This is only approximately 6 points per wavelength.

The computations are conducted using two methods: the IMM and the solid wall boundary conditions developed by Tam and Dong [6]. The thickness of the plate is Δy in the IMM, and zero in the solid wall boundary condition method. The pressure on the two sides of the plate is different, so in the IMM at least one Δy of thickness is needed. That is, in two rows of length L, the mean density equals $1/30$. When an acoustic wave train impinges on the plate, the wave is scattered. In the shadow region behind the plate, acoustic waves radiated directly from the source are blocked so the sound pressure consists only of the contributions

from waves diffracted by the two sharp ends of the plate. Figure 10 shows the pressure contours computed using the IMM at time $t = 194$. The diffraction pattern behind the plate and the scattering pattern in front of the plate can be seen clearly. Figure 11 shows the corresponding pressure distributions along the upper boundary of the computational domain obtained from both the IMM and Tam and Dong's method [6]. The agreement between the two solutions is very good. The computing time for the IMM is two-thirds that for Tam and Dong's method. Also, the coding in the IMM is extremely simple. In the IMM, the amount of coding work and the computing time do not change at all when there is an solid object present. This is one of the major advantages of the IMM.

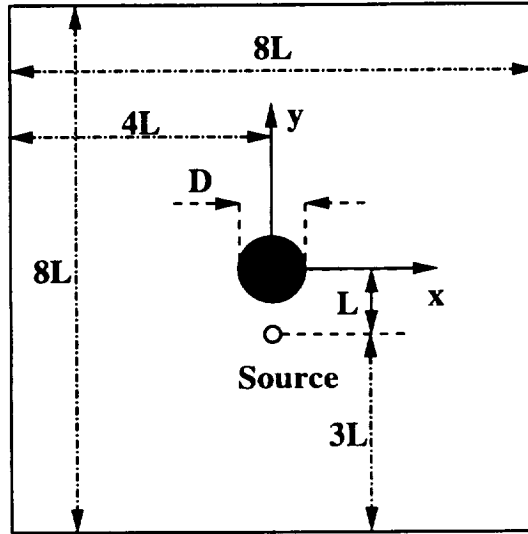### 4.4. *Acoustic Scattering of Time Periodic Acoustic Waves By A Circular Cylinder*

Fig. 12. Sketch of Computational Domain for Circular Cylinder Scattering Problem

The scattering of a periodic acoustic wave train by a circular cylinder is considered next. This is sketched in figure 12. The computational domain is 201 by 201. The cylinder is placed at the center of the domain and has a diameter $D = 25$. The acoustic wave train is still generated by a time periodic source in the energy equation. The source and its location are the same as those described in section 4.2.

The important difficulty in this example is how to deal with the curved solid boundaries. Uniform Cartesian grids and high-order finite difference DRP schemes have been used throughout this paper. The use of a uniform grid has advantages in the maintenance of good dispersion and dissipation properties, as does the high-order finite difference DRP scheme. However, their use also presents a problem. This is the non-conformity of the grids with the boundaries of curved bodies. Kurbatskii and Tam [4] have recently introduced a technique for Cartesian treatment of curved walls for high-order finite-difference schemes. In the present calculations we used the nearest grid points to the boundary to define the body shape. So the curved boundary is approximated by a staircase boundary. This results
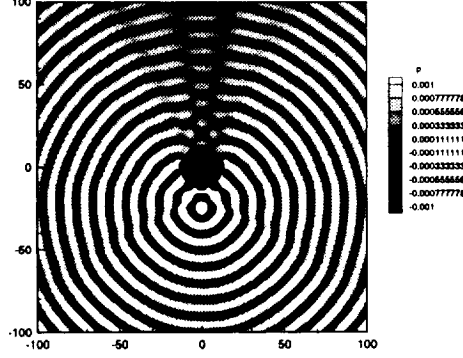
Fig. 13. Pressure Contours at $t = 180$ for Scattering of Periodic Source by a Circular Cylinder. $D = 25$.
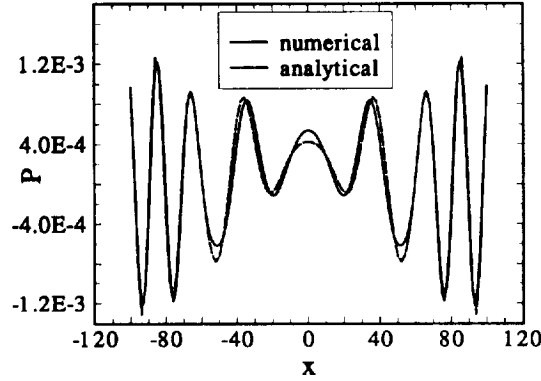

Fig. 14. Pressure Distribution Along Upper Boundary of Computational Domain for Scattering of Periodic Source by a Circular Cylinder

in some errors in the computation. But, as demonstrated in the following example, this error may be small if the IMM is used. For the circular cylinder, the wall region is defined as $(x^2 + y^2)^{1/2} \leq D/2$. Inside this region, the mean density is set equal to $1/30$. This is all that is needed in order to define the presence of the cylinder. After this the computations are carried out directly. It is obvious that the coding work and computing time are the same with or without the object. Also, there is no difference at all if the boundary is curved or flat. This is the most important advantage of the IMM.

Figure 13 shows the pressure contours computed at time $t = 180$. The scattering pattern behind and in front of the cylinder is seen clearly. Figure 14 shows the pressure distribution along the upper boundary of the computational domain. The analytical solution is also shown. The agreement between the computed and analytical results is good. It can be concluded that the use of a stair-stepped surface to approximate the curved boundary is a reasonable approximation in the IMM. Since in the IMM the position of the object surface

could be anywhere in a range of one grid spacing, this has a smoothing effect on the staircase surface and makes the surface approximation more accurate. It can be seen that the IMM is a very efficient and convenient method to treat curved boundaries.

5. Acoustic Reflection and Scattering From 3-D Bodies

In this section, two problems of acoustic scattering by three-dimensional bodies are solved using the IMM. The first problem is the acoustic scattering of a time periodic acoustic wave by a sphere. This is an axisymmetric 3-d problem. The analytic solution is given by Morris [5] and is compared with the numerical solutions. The second problem is acoustic radiation and scattering from a cylindrical shell with a acoustic source placed inside the shell. No analytical solutions are available for this problem, so that only numerical results are presented.

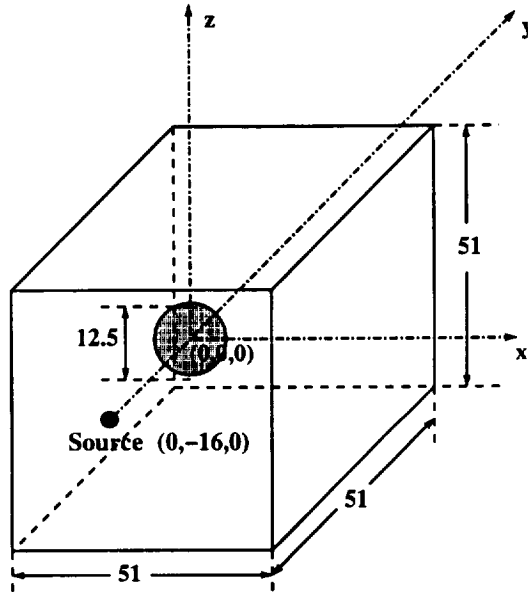### 5.1. *Acoustic Scattering of Time Periodic Acoustic Waves By A Sphere*

Fig. 15. Sketch of Computational Domain for Sphere Scattering Problem

The scattering of a periodic acoustic wave train by a sphere is considered as shown in figure 15. The domain is 51x51x51. The sphere is placed at the center of the computational domain. This is also the origin of the coordinates. The sphere diameter is $D = 12.5$. The acoustic wave train is generated by a time periodic source in the energy equation. The source term has the form

$$H = 0.01 \exp\{\frac{\ln 2}{(25/8)^2}[x^2 + (y + 16)^2 + z^2]\}$$

$$\cos(\omega t) \tag{5.14}$$

ω is the angular frequency. 10 points per wavelength are used, so that $\omega = \pi/5$. The center of the source is at (0,-16,0).
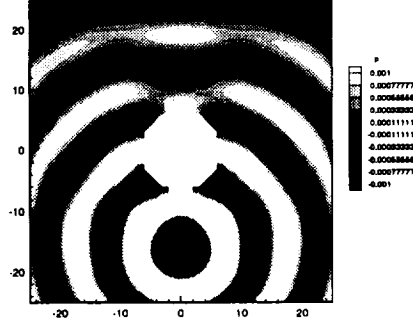

Fig. 16. Pressure Contours at $t = 45$ for Scattering of Periodic Source by a Sphere.

The sphere is the wall region, which is defined by $\sqrt{x^2 + y^2 + z^2} \le D/2$. Inside this region, $\rho_0 = 1/30$. It is clear that the boundary of the sphere is approximated by a staircase boundary. Figure 16 shows the computed pressure contours at the $z = 0$ section at time $t = 45$. This section passes through the center of the sphere. The scattering pattern behind and in front of the sphere is clear. Figure 17 is the pressure waveform along the x-axis at this section and at the same time. Figure 18 is the pressure waveform along the y-axis. The numerical results may be compared with the analytical results and good agreements are achieved. Most of the disagreement occurs because of the relatively coarse grid used in this simulation.

This numerical example demonstrates that the IMM is applicable to 3-d acoustic scattering problems. The coding work would be tremendous if the traditional solid wall boundary conditions were used for 3-d scattering cases. For the IMM, there is no extra coding work and computation time at all when the 3-d scatterers exist.

5.2. *Acoustic Radiation and Scattering of Time Periodic Acoustic Waves Inside A Cylindrical Shell*

As a final example, the radiation and scattering of a periodic acoustic wave train inside a cylindrical shell is considered. The acoustic wave train is generated by a time periodic source in the energy equation, the same as that in section 5.1, located at (0,0,0). The domain is 51x51x51. The shell is placed at the center of the domain. The inner radius of the shell is $r_1 = 6.25$, the outer radius is $r_2 = 9.25$. The thickness of the shell is 3. The length of the shell is $h = 26$ and the axis of the shell aligns with z-axis. The computational domain is sketched in figure 19.

The wall of the shell is defined as $r_1 \le \sqrt{x^2 + y^2} \le r_2$, and $|z| \le 13$. Inside this region $\rho_0 = 1/30$. So the inner and outer boundaries of the shell are all approximated by staircase boundaries. As an example of the calculated pressure contours figure 21 shows the pressure
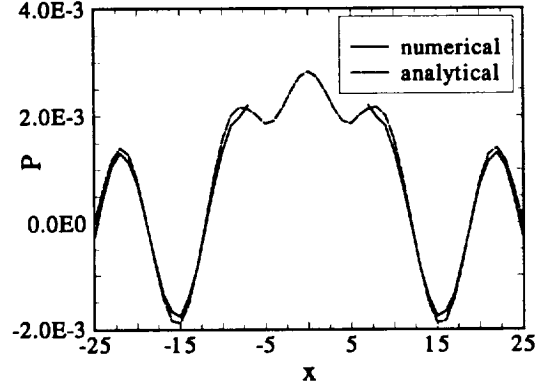
Fig. 17. Pressure Distribution Along x-axis at time $t = 45$ for Scattering of a Periodic Source by a Sphere.
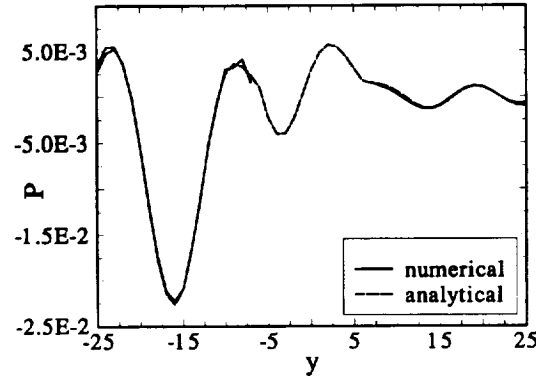

Fig. 18. Pressure Distribution Along y-axis at time $t = 45$ for Scattering of a Periodic Source by a Sphere.

contours at section $y = 0$, which cuts through the center of the shell. It can be seen that when an acoustic source is placed inside the shell, the acoustic waves can radiate from the two open ends. These two open ends diffract waves and act like sources for the external acoustic field. Outside the shell the pressure field is stronger closer to the ends, and weaker away the ends. Inside the shell a standing wave pattern can be seen

This numerical simulation demonstrated that the IMM can deal with various kinds of 3-d objects very easily. The complex geometries, so long as they reasonably smooth, do not represent any difficulty in the IMM.

6. Conclusions

In this paper we have introduced an efficient method to simulate solid wall boundaries, the Impedance Mismatch Method. This method was applied to a number of 2-d and 3-d
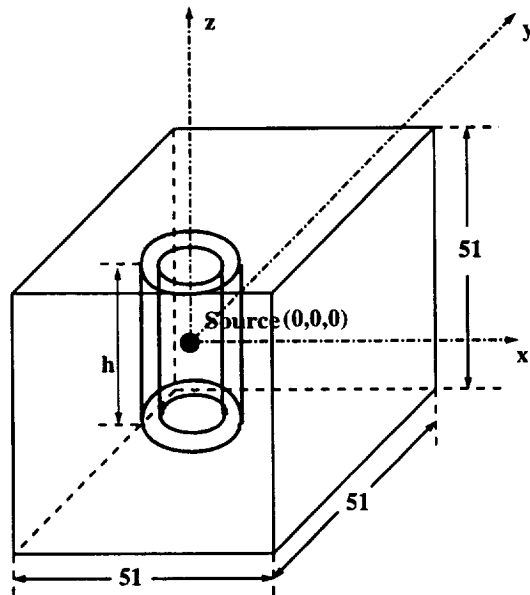
Fig. 19. Sketch of Computational Domain for Shell Scattering Problem

scattering problems with both flat and curved boundaries. Many advantages of the IMM have been found and demonstrated. No special solid wall boundary conditions need to be implemented. No stencil changes are involved because of the presence of solid objects and the coding is very easy. The computations are much faster than when the traditional solid wall boundary treatments are used. There is no difficulty for any reasonable smooth geometry. No matter whether the solid boundary is flat or curved, the amount of coding work and computing time are the same. Some disadvantages of the IMM have also been revealed. The accuracy of the computations depends on the value of the mean density ratio in the wall region. Also there is an one-grid-size error in the wall position. An extra wall region is needed for the infinite wall case. Finally, a staircase approximation is used to approximate curved boundaries. This paper has demonstrated that the IMM is a promising method for the simulation of acoustic reflection, scattering, and diffraction problems.

Acknowledgements

References

[1]   Chung, C., "Wave propagation and scattering in computational aeroacoustics", Ph.D. Thesis, The Pennsylvania State University, 1995.

[2]   Huh, K. S. Agarwal R. K. and Widnall S. E., "Numerical simulation of acoustic diffraction of two-dimensional rigid bodies in arbitrary flow," *AIAA Paper* 90-3920 (1990)
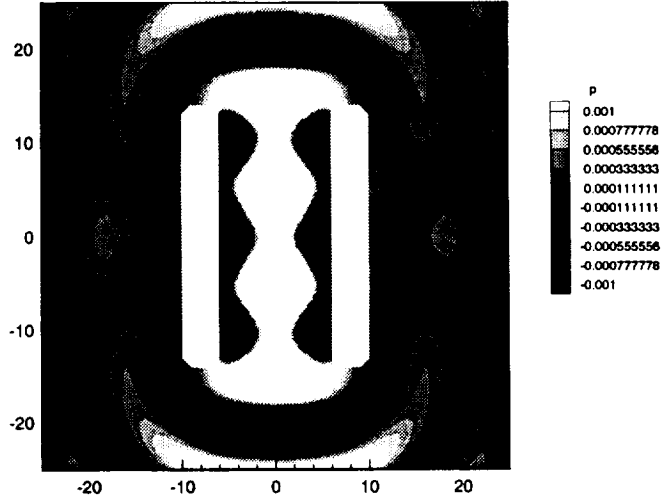
Fig. 20. Pressure Contours at $t = 45$ for Shell Radiation and Scattering Problem on $y = 0$ Section.

[3]   Khan, M. M. S., Brown, W. H. and Ahuja, K. K., "Computational aeroacoustics as applied to the diffraction of sound by cylindrical bodies," *AIAA Journal* **25**(7) (1987) 949–956.

[4]   Kurbatskii, K. A. and Tam, C. K. W., "Cartesian boundary treatment of curved walls for high-order computational aeroacoustics finite difference schemes," *AIAA Paper* 96-0275 (1996)

[5]   Morris, P. J., "The scattering of sound from a spatially-distributed spherically-symmetric source by a sphere," *J. Acoustical Society of America* **98**(6) (1995) 3536–3539.

[6]   Tam, C. K. W. and Dong, Z., "Wall boundary conditions for high order finite difference schemes in computational acoustics," *Theoretical and Computational Fluid Dynamics* **6** (1994) 303–322.

[7]   Tam, C. K. W. and Webb, J. C., "Dispersion-relation-preserving finite difference schemes for computational acoustics," *J. Computational Physics* **107** (1993) 262–281.

NUMERICAL PREDICTION OF THE NOISE PRODUCED BY A PERFECTLY EXPANDED RECTANGULAR JET

Thomas S. Chyczewski* and Lyle N. Long†
Department of Aerospace Engineering
The Pennsylvania State University, University Park, PA 16802

Abstract

Supersonic rectangular jet flow and far field noise predictions are made by solving the governing equations using advanced numerical techniques on parallel processors. The computational domain begins at the jet nozzle exit and contains the jet plume and a small region of the acoustic near field. The equations solved for the interior grid points are the full 3D Navier Stokes equations. The far field boundary points are determined by unsteady, nonlinear characteristic based nonreflecting conditions. To model the jet nozzle exit flow, a set of equations are developed to simulate many features of this flow that have been experimentally observed to influence the jet and its radiated noise. A Kirchhoff method is used to determine the far field noise from information extracted from the finite computational domain. Each set of governing equations is spatially discretized by a sixth order central difference scheme and advanced in time using fourth order Runge-Kutta integration. Spurious high wave number fluctuations are damped by a nonlinear dissipation algorithm that has a minimal effect on the acoustic solution. The code has been efficiently implemented on the CM5 using CMFortran (essentially HPF) and should be easily ported to platforms running HPF (such as the SP2). Numerical results indicate that the algorithm, which contains no model constants (aside from the nozzle exit conditions), is capable of reproducing many experimentally observed rectangular jet flow and noise features.

1   Introduction

Jet noise analysis and reduction have been topics of research since the introduction of the jet engine as a propulsion device for aircraft during World War II. Many tools have been developed and incorporated into the design process to reduce the annoyance of jet noise. The Federal Aviation Administration began placing

strict regulations on the noise produced by aircraft[1] and this has caused a renewed interest in noise prediction in the scientific community. This is particularly true in light of the national interest to develop the High Speed Civil Transport (HSCT). Noise reduction is considered to be a crucial technology required for a viable design.

The prediction strategy that is currently receiving the most attention is direct simulation. Jet noise research has included many different implementations of this approach.[2-5] The implementation under investigation in this paper solves the 3D full Navier Stokes equations in a domain that includes the noise source region and a small portion of the acoustic field. The acoustic near field solution is then used as an input to a Kirchhoff method to determine the far field noise.

Consistent with experimental evidence,[6,7] the noise source is assumed to be dominated by the evolution of large scale coherent structures in the jet shear layer and thus only these scales are resolved. The influence of the small scales is assumed to be represented by numerical dissipation. Thus, no turbulence model is employed and consequently, there are no adjustable model constants used in the interior domain.

The computational domain in which the Navier Stokes equations are solved begins at the jet nozzle exit plane. A model is therefore required for the nozzle exit flow and can have an appreciable effect on the numerical solution. The effects of nozzle exit conditions on experimental and numerically simulated jets have been studied by many investigators.[8-15] Hussain and Husain[8] found experimentally that the development of the jet depends on the nozzle boundary layer momentum thickness distribution. The azimuthal variation has been shown by them to produce noticeable effects on the spreading rate of elliptic jets. These effects are the result of the influence of the momentum thickness on the generation of coherent structures. King et al.[12] found that nozzle imperfections as small as 0.2% of the nozzle exit diameter may have a significant effect on the development of supersonic axisymmetric jets. They used this information to develop methods of enhancing jet mixing. The initial turbulence intensity was found have a significant effect on the turbulence amplification rate

---

*Doctoral Candidate, Member, AIAA

†Associate Professor, Senior Member, AIAA

in the near-field region of the jet by Grinstein et al.[11] Quinn[14] found differences in the spreading rate of two jets operating under essentially the same flow conditions and geometry. These discrepancies were attributed to facility differences.

This experimental evidence suggests that the salient features of a laboratory facility will have an appreciable effect on the development of a jet. These effects can be observed in the form of varying potential core lengths, turbulence levels and jet spreading rates. To compound this potential problem, the nozzle exit conditions of the rectangular jet simulated in this paper are not defined precisely. The measurement techniques available to Kinzie[16] did not permit a comprehensive study of the nozzle exit. Due to this uncertainty, a general model for the nozzle exit flow has been developed that can turn on or off some of the features that have been observed to significantly influence the jet development. The results presented in this paper are confined to studying the effect of modal excitation. The effects of nozzle exit turbulence levels and corner vortices are discussed in Chyczewski(1996).[17]

Since the computational domain is limited to just a small region of the acoustic near field, a method is required to extrapolate the solution to the far field. In this work the Kirchhoff method is employed.[18] It consists of constructing a surface S on which the acoustic solution can be reliably calculated. The acoustic solution at any location outside of this surface can then be determined by the Kirchhoff formula. The solution is exact for sound radiation outside of a surface S if that radiation is governed by the convective wave equation. However, in the application of this method to the jet noise problem, finding such a surface is difficult. This issue has been addressed previously by some investigators who have found that the far field solution is not very sensitive to the location of the surface if some precautions are taken. Lyrintzis and Mankbadi[19] found that placing the surface at least one diameter away from the jet centerline is sufficient to obtain accurate solutions. Freund et al.[20] performed a study analyzing the effects of using open Kirchhoff surfaces and found that it does not introduce significant errors if the surface passes through the region between the noise source and the observer.

In the next section, the governing equations are described. This consists of discussing the specific form of the Navier Stokes equations, presenting the boundary equations, which includes the model nozzle exit conditions, and finally presenting the Kirchhoff formulation used here. In section 3 the numerical approach is outlined. Special attention is given to the artificial dissipation model. Next, in section 4, rectangular jet noise prediction results are presented and compared to experimental data. Finally, in section 5, some conclusions are drawn.

2 Governing Equations

A supersonic rectangular jet flow is a nonlinear, viscous, unsteady, 3D problem. As such, it is governed by the full, compressible, 3D Navier Stokes equations. A nondimensional conservative form of these equations is used in this work (see Hoffmann(1989)[21]). By themselves, these equations are not sufficient to model the jet problem. Boundary conditions are required to allow flow and acoustic waves to pass through the far field boundaries of the computational domain as well as to model the flow entering the domain from the nozzle exit. This section presents these equations as well as the Kirchhoff formulation used to extrapolate the acoustic solution to the far field.

2.1 Nonreflecting Boundary Conditions

Several approaches to the specification of nonreflecting conditions at far field boundaries have been developed. These approaches can be classified into three categories: asymptotic solutions,[22,23] Fourier decomposition[24,25] and quasi one-dimensional analysis.[26,27] The most recent set of conditions based on the asymptotic solution of the linearized Euler equations are due to Tam and Webb.[23] These asymptotic conditions have been quite successful at reducing boundary reflections for many model problems.

Giles[24] derived approximate unsteady boundary conditions for two-dimensional problems by performing a Fourier decomposition of the linearized Euler equations. They have been applied to turbomachinery problems by Giles and have been found to be effective. When implemented with a buffer zone, these conditions have been able to permit nonlinear vortical structures to leave a computational domain with little reflection.[25]

A drawback of both the asymptotic and Fourier methods is that their derivation employs a set of equations that have been linearized with respect to a reference solution. In many cases, such as the rectangular jet problem under consideration here, the reference solution is not known a priori and must be developed as the equations are integrated. Experimentation with the rectangular jet problem suggests that asymptotic and Fourier methods are not capable of establishing a reasonable reference, or time averaged, solution when the initial condition is a quiescent fluid.

Given this difficulty, the quasi one-dimensional boundary procedure developed by Thompson[26,27] is employed. The approach consists of decomposing the full nonlinear Euler equations into modes of definite velocity and specifying nonreflecting conditions for those modes that have a velocity directed into the computational domain. These conditions have been shown to be able to allow large amplitude disturbances to leave the domain with little reflection.[26]

2

2.2 Nozzle Exit Conditions

A complete prescription of the nozzle exit conditions requires the specification of both steady and unsteady characteristics. They are described in the following two subsections.

2.2.1 Steady Nozzle Conditions

A nearly uniform velocity profile was found at the nozzle exit by Kinzie.[16] This indicates that viscous effects are confined to locations very close to the nozzle wall. Thus the simulated jets use uniform profiles for density, axial velocity and pressure. Accurate measurements of momentum thickness variations that may exist around the nozzle lip were not performed and are thus not accounted for in the nozzle model.

The values of the exit variables are found from the experiment. The exit Mach number, M_j, is 1.54, the acoustic speed of the jet is $\bar{c}_j = 0.82 c_\infty$ and since the jet is ideally expanded, the jet exit pressure is the same as the ambient pressure ($\bar{p}_j = p_\infty$). From this information, the steady exit density and velocity can be found. In this paper, the nozzle exit flow is assumed to be purely axial. The effects of lateral exit flow components induced by nozzle exit corner are considered in Chyczewski(1996).[17]

2.2.2 Unsteady Nozzle Conditions

There is a very limited amount of information available in the literature that discusses the unsteady features of a supersonic nozzle exit flow. In fact, the authors have not seen any published data that characterizes the unsteady features to the extent that is required to reproduce the nozzle exit conditions completely. This is most likely due to the extreme difficulty of collecting such data.

To compensate for this lack of information, a general set of unsteady nozzle exit conditions have been developed that can specify the disturbance spatial distribution, amplitude, temporal behavior and phase relation around the nozzle lip. By controlling the phase relation, different modes (flapping or varicose) can be excited at the nozzle exit. This is similar to the artificial excitation used by many experimentalists.[7,16,28-30] With this model, many different features can be investigated. In this paper, the investigation is confined to studying the modal excitation.

The velocity perturbations are calculated from the following relation :

$$u', \quad v' \quad or \quad w' = \frac{u_j}{2}\alpha \sum_{i=1}^{4} c_i A_i \sum_{l=1}^{2} \sin(2\pi f_l t + \phi_l^n + \beta_i) \quad (1)$$

The contributions of each of these terms is given in the following sections.

Temporal Behavior.

The inner summation in equation 1 is over contributions from two characteristic frequencies. These two frequencies are the screech tone frequencies found in the minor axis plane of the experimental jet.[16] These frequencies can also be determined using the linear shock cell model and weakest link theory developed by Tam.[31] For our problem these frequencies are $f_1 = 9606$ Hz (Strouhal number = 0.31) and $f_2 = 26367$ Hz (Strouhal number = 0.84).

A random component to the excitation is supplied by ϕ_l^n in equation 1. It is initialized to zero at the beginning of each run. It is then updated at each timestep, n, by the following :

$$\phi_l^n = \phi_l^{n-1} \pm \theta \quad (2)$$

The amplitude of the phase shift between time steps θ is 5.4 degrees. This value was found to give broad frequency spectra with an upper band limit that is near the highest frequency that the grid and scheme can resolve.

Spatial Distribution.

The perturbation on the entire nozzle lip is determined by building it up from the contributions of the four walls. This is done in equation 1 by the outer summation. A_i is the spatial amplitude function for each of the walls. It is a Gaussian function centered on the lip line of each wall. The half width of the Gaussian is one tenth of the short dimension of the nozzle. The function is tapered to zero amplitude near the corners of the nozzle. This spatial function is selected since a Gaussian is a representative distribution for wall bounded shear layer perturbations (see Kinzie(1995)[16] for example).

Mode Excitation.

Two different modal excitations are considered in this paper. These are the varicose and flapping modes and have been found in the experimental jet by Kinzie.[16] The varicose mode is characterized by symmetric shedding of coherent structures from the nozzle lip. In contrast, the vortex shedding is asymmetric for the flapping jet case. This is illustrated in figure 1. These different modes are excited in the jet by controlling phase differences between the walls of the nozzle. The phase difference is controlled by the angle β_i in equation 1. Whether or not there is a velocity component contribution to the perturbation from a wall is determined by the parameter c_i. The values of these two parameters for each of the velocity components is given in tables 1 and 2 for the varicose and flapping modes.

The final parameter in equation 1 is α. It specifies the peak amplitude of the velocity perturbation. A value of 0.02 is used and corresponds to an RMS fluctuation level near 1.36 percent of the exit velocity. The
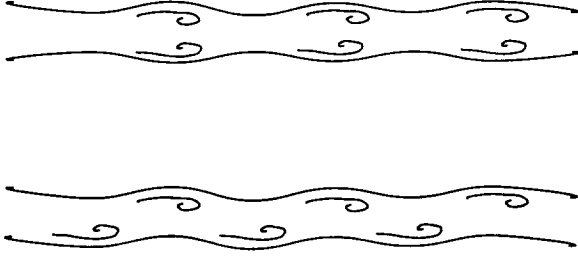
Figure 1: Vortex shedding in varicose (top) and flapping (bottom) excited jets.

	c_1	c_2	c_3	c_4	β_1	β_2	β_3	β_4
u'	1	1	1	1	0	0	0	0
v'	1	0	1	0	$\frac{\pi}{2}$	0	$-\frac{\pi}{2}$	0
w'	0	1	0	1	0	$-\frac{\pi}{2}$	0	$\frac{\pi}{2}$

Table 1: Values of c_i and β_i for varicose mode excitation.

RMS levels vary slightly from run to run due to the random nature of the excitation.

The instantaneous velocities are obtained by adding the steady contribution to the perturbation. Given these velocities, the pressure and density are found from conditions of constant total temperature and entropy. The first condition was found to be reasonable for a jet flow under these conditions by Troutt and McLaughlin.[32] The assumption of isentropic excitation is justified since these perturbations most likely originated from acoustic disturbances upstream of the nozzle exit.

2.3 Kirchhoff Formulation

The moving surface formulation given by Farassat and Myers[18] for a rigid surface in rectilinear motion is employed. It gives the acoustic pressure p' at location $\vec{x}$ and time t as a function of the pressure on a suitably defined surface S (where $\vec{x}$ is outside of S):

$$4\pi p'(\vec{x}, t) = \int\!\!\int_S \left[\frac{E_1}{r(1 - M_r)}\right]_{\tau^*} dS \qquad (3)$$

$$+ \int\!\!\int_S \left[\frac{p' E_2}{r^2(1 - M_r)}\right]_{\tau^*} dS \qquad (4)$$

where

$$r = |\vec{r}|, \quad \vec{r} = \vec{x} - \vec{y}(\tau), \quad M_r = \vec{M} \cdot \vec{r}/r, \qquad (5)$$

$$E_1 = -\vec{n} \cdot \nabla p' + (\vec{M} \cdot \vec{n})(\vec{M} \cdot \nabla p') \qquad (6)$$

$$+ \left[\frac{\cos\theta - \vec{M} \cdot \vec{n}}{c_\infty(1 - M_r)} - \frac{\vec{M} \cdot \vec{n}}{c_\infty}\right]\frac{\partial p'}{\partial \tau}, \qquad (7)$$

	c_1	c_2	c_3	c_4	β_1	β_2	β_3	β_4
u'	1	0	1	0	0	0	π	0
v'	1	0	1	0	$\frac{\pi}{2}$	0	$\frac{\pi}{2}$	0
w'	0	0	0	0	0	0	0	0

Table 2: Values of c_i and β_i for flapping mode excitation.

$$E_2 = \frac{1 - M^2}{(1 - M_r)^2}(\cos\theta - \vec{M} \cdot \vec{n}) \qquad (8)$$

M is the Mach number of the moving surface which for the static jet problem is zero. The vector $\vec{r}$ is the vector difference between the observer location and the location of the Kirchhoff surface element (it varies with each location on the surface). $\vec{n}$ is the normal vector pointing out of the Kirchhoff surface, the angle θ is measured between the vectors $\vec{r}$ and $\vec{n}$, and c_∞ is the freestream sound speed. The integrands are evaluated at the Kirchhoff surface emission time τ^* which, for a stationary surface, is given by

$$\tau^* = t - r/c_\infty \qquad (9)$$

A complete description of the coupling of the Kirchhoff method into the Navier Stokes code is given in Ozyoruk and Long[33] and is therefore not described here.

3 Numerical Algorithm

The governing equations are discretized in a finite difference context using fourth order accurate Runge-Kutta time integration and sixth order accurate spatial discretization. The computational domain is illustrated in figure 2 which also shows the coordinate system. The center of the nozzle exit is located at $(x, y, z) = (0, 0, 0)$. Details on the grid generation strategy can be found in Chyczewski and Long(1995)[34] and Chyczewski(1996).[17]

3.1 Artificial Dissipation

A desirable feature of this numerical algorithm is the explicit control of the amount of dissipation applied to the scheme. Unlike upwind methods, Runge Kutta - central difference techniques contain very little implicit dissipation. Instead, explicit filters are used for stability and to prevent odd-even decoupling errors. Selection of an appropriate dissipation scheme is paramount in calculations where one wishes to extract the low amplitudes and high frequencies associated with acoustics. Jameson et al.[35] proposed a blend of split second and fourth order dissipation. While this dissipation is robust near discontinuities, it may significantly contaminate the acoustic solution.
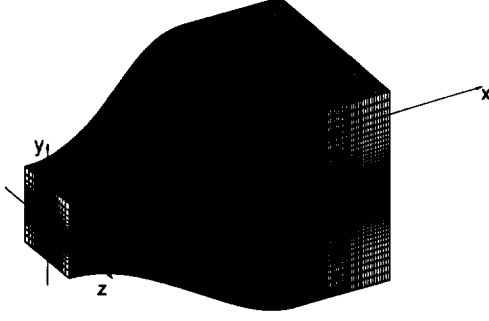
4

Figure 2: Three dimensional view of the grid.

A combination of second and sixth order dissipation is used here. This dissipation has been applied to the nonlinear acoustic benchmark problems[34] and has proven capable of propagating acoustic waves in the presence of strong discontinuities. It is applied to the scheme as a correction to the residual and takes the following form :

$$\mathcal{D}(\mathbf{Q})_{i,j,k} = \mathcal{D}_\xi(\mathbf{Q})_{i,j,k} + \mathcal{D}_\eta(\mathbf{Q})_{i,j,k} + \mathcal{D}_\zeta(\mathbf{Q})_{i,j,k} \quad (10)$$

Each term is determined as follows (using $\mathcal{D}_\xi$ as an example) :

$$\mathcal{D}_\xi(\mathbf{Q})_{i,j,k} = \epsilon^{(2)}\mathcal{D}_\xi^2(\mathbf{Q})_{i,j,k} + \epsilon^{(6)}\mathcal{D}_\xi^6(\mathbf{Q})_{i,j,k} \quad (11)$$

where

$$\mathcal{D}_\xi^2(\mathbf{Q})_{i,j,k} = \frac{1}{J\Delta t}(\mathbf{Q}_{i+1,j,k} - 2\mathbf{Q}_{i,j,k} + \mathbf{Q}_{i-1,j,k}) \quad (12)$$

and

$$\mathcal{D}_\xi^6(\mathbf{Q})_{i,j,k} = \frac{1}{J\Delta t}(-20\mathbf{Q}_{i,j,k} + 15(\mathbf{Q}_{i+1,j,k} + \mathbf{Q}_{i-1,j,k})$$
$$-6(\mathbf{Q}_{i+2,j,k} + \mathbf{Q}_{i-2,j,k}) + (\mathbf{Q}_{i+3,j,k} + \mathbf{Q}_{i-3,j,k})) \quad (13)$$

The coefficients are determined in a manner very similar to that used by Jameson:

$$\epsilon_i^{(2)} = k^{(2)}\max(\nu_{i-1}, \nu_i, \nu_{i+1}) \quad (14)$$

and

$$\epsilon_i^{(6)} = \max(0, k^{(6)} - \epsilon_i^{(2)}) \quad (15)$$

where the values of $k^{(2)}$ and $k^{(4)}$ used here are 1.5/4 and 1.5/256, respectively. The flow gradient sensor ν is given by

$$\nu_i = \frac{|\beta_{i-1,j,k} - 2\beta_{i,j,k} + \beta_{i+1,j,k}|}{\beta_{i-1,j,k} + 2\beta_{i,j,k} + \beta_{i+1,j,k}} \quad (16)$$

β is set equal to the total pressure. The Jameson scheme[35] uses the static pressure. For our jet calculations, the highest flow gradients are found near the jet exit. Since the static pressure is essentially uniform there (ideally expanded jet), using the static pressure is inappropriate.

The second order dissipation coefficient, $\epsilon^{(2)}$, is explicitly set to zero in regions where the flow is sufficiently smooth, i.e. ν is below a specified value. To minimize the size of the region with second order dissipation, this value should be raised to a maximum that results in a stable scheme. An appropriate value has been determined to be 0.0050 by numerical experimentation. The locations where the second order dissipation is necessary is found to be confined to certain locations in the jet core and should have no effect on the radiated acoustic solution. This is illustrated in figure 3 where a snapshot of the locations in the minor plane where second order dissipation is applied at a typical instant.
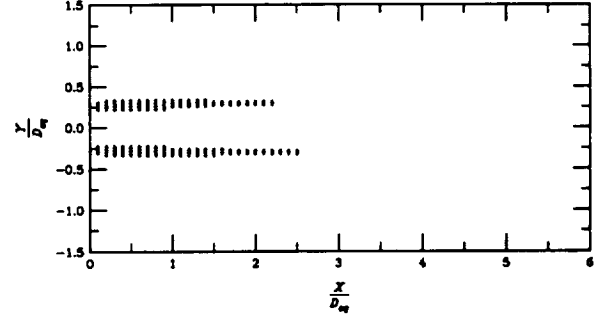

Figure 3: Snapshot of the locations in the minor axis plane where second order dissipation is applied.

4   Results

In this section, rectangular jet simulation results are presented and compared to experimental data. The results are obtained by executing a run that consists of three phases. Since the initial condition of the simulation is a quiescent fluid, one phase is required to allow transients to leave the domain and establish the jet. When the domain is free of transients, the Kirchhoff integration is started. There is a transient convergence period required by Kirchhoff methods which is based on the furthest distance between the Kirchhoff surface and an observer location.[33] The time required to converge the Kirchhoff solution constitutes the second phase. The final phase is used to sample variables in the jet and in the near and far acoustic fields. Only the data collected in the last phase has been used to generate the results presented here.

Figure 4 shows the centerline velocity distributions for the varicose and flapping excited jets and compares them to the experimental data.[16] The varicose jet simulation results are shifted $-2D_{eq}$ to match the potential

5

core length of the experiment. This common procedure is used so that the decay rates of the centerline velocity can be compared directly. This shift is applied to all comparisons of the varicose excitation simulation with experimental data presented throughout this paper. The flapping excited jet does not require a shift.
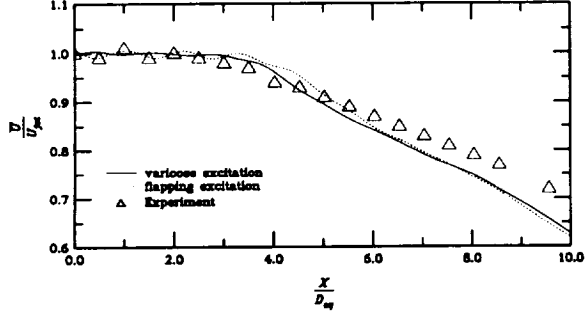

Figure 4: Centerline velocity distributions.

The comparison between the simulations and experiment after the end of the potential core shows that the simulation overpredicts the turbulent mixing slightly for both of the mode excitations since their centerline velocities decay at a faster rate. A distinguishing feature between the two simulation profiles is that the flapping excitation case has noticeable oscillations in the potential core region. These oscillations, also present in the experimental data, are due to a shock cell structure. They are also present to a lesser degree in the varicose excitation case profile. In the experimental jet, this structure most likely originates in the throat of the nozzle as a result of an imperfect nozzle design.

Recall that the static pressure prescribed by the steady nozzle exit conditions is set to the ambient pressure; however, superimposed on this steady condition are perturbations. These perturbations are likely responsible for the weak shock cell structure found in the simulated jet. Why the flapping mode excitation produces a stronger shock cell structure is not understood. It is interesting to note, however, that the simulation reproduces fairly accurately the amplitude, wavelength and phase of the shock cell structure (given the limited resolution of the experimental data). This may suggest that the mechanisms producing the shock cell structures in both jets are similar and that the experimental shock cell structure is not solely due to an imperfect nozzle design.

Since the evolution of large scale turbulent structures plays such an important role in supersonic jet noise generation, some of the simulated properties of these structures have been determined and compared to experimental data. In his experiment, Kinzie[16] used hot wire anemometry to measure the fluctuations in the shear layer. In a compressible flow, these wires are sensitive

to the mass flux that is normal to the wire. Measurements were made in both the major and minor axis planes of the jet. When performing major axis plane measurements, the hot wire was oriented parallel to the minor axis plane, i.e., it was parallel to the wall from which the shear layer was emanating. This was done to improve the resolution of the shear layer measurements. When arranged in this manner, the normal component of the mass flux consists of two velocity components, i.e., the hot wire is sensitive to :

$$m = \sqrt{(\rho u)^2 + (\rho w)^2} \qquad (17)$$

Figure 5 shows the axial development of the RMS of the variable m defined in equation 17 (normalized by the jet exit mass flux) in the major axis plane. The values plotted in the figure are the maximum RMS values through the shear layer for a given axial location.
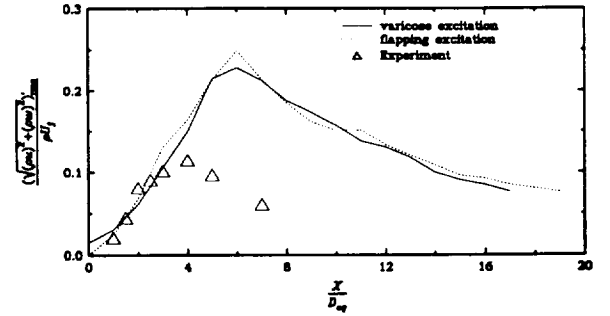

Figure 5: Maximum RMS levels of the mass flux normal to the hot wire in the major axis plane.

The most apparent observation made from this figure is that the simulation over predicts the peak amplitude of the perturbations by approximately a factor of 2. Thus, there is significantly more turbulent mixing in the simulated jet compared to the experimental one. This is consistent with the centerline velocity decay profile presented earlier. A possible explanation for this discrepancy is the absence of a sub-grid-scale (SGS) turbulence model. In turbulent flow, the large scales of the turbulence are continually acted on by the finer scales. These fine scales behave as a dissipation mechanism for the larger scales. The algorithm used in this research does not address this issue explicitly. The algorithm applied here relies on the dissipation supplied by the numerical scheme to behave like the sub-grid scales of the true flow. The difference between the artificial and SGS dissipation is quantified in Chyczewski(1996)[17] and will not be discussed in detail here. It will just be mentioned that a comparison of these two dissipation terms reveals that the SGS dissipation is usually larger than the artificial dissipation but the difference is not considered significant enough to account for the discrepancies found here. The high amplitude perturbation found in the simulation may also be explained by the nozzle exit

conditions. Berman et al.[36] found that changing the exit conditions for their subsonic calculations can reduce the peak amplitude of the perturbations.

Aside from the peak amplitude discrepancy, a comparison of the trends in figure 5 between the simulation and the experiment is encouraging. There is a high amplitude growth rate prior to the end of the potential core, the value of which compares well between experiment and simulation. After this region, there is a saturation period and finally a gradual decay in the amplitude.

The power spectral density of the time series used to determine the RMS values discussed above for the varicose excitation in the major axis is presented in figure 6. The sample used to determine these spectra spans the final phase of the run described at the beginning of this section. This phase consists of 32,768 timesteps. In order to make handling the data less cumbersome, a sample was taken once every 16 timesteps. This procedure compromises no information since the sampling frequency is still much higher than the frequencies expected to be produced by the jet. Thus, the length of the entire sample is 2048 steps. To reduce the errors associated with using a finite (and relatively small) sample record, the 2048 sample is divided into 15 records that contain 256 steps. The intervals overlap one another by 128 elements. For example, the first interval contains samples 1 through 256, the second contains 129 through 384, and so on. The spectra presented in figure 6 are obtained by averaging the spectra obtained from each of the 15 intervals. A Hanning window is also used to reduce the errors associated with the finite record length (see Bendat(1986)[37] for example). Since the area under the power spectral density is equal to the RMS of the fluctuation, which have been previously discussed, the experimental spectra have been scaled so that they have RMS values equal to the simulation. This allows a direct comparison of the spectral distribution of energy. The spectra are presented as a function of the Strouhal number, which is the ratio of the frequency to a characteristic frequency. The characteristic frequency used in these spectra is 31387 Hz, which is the experimental jet exit velocity divided by the equivalent diameter of the nozzle exit.[16]

The comparison between the experimental and simulation spectra is favorable. In both the experiment and the simulation the energy moves to lower frequencies at the larger axial locations. This also agrees with observations made by Troutt.[29] The spikes in the major axis experimental spectra near a Strouhal number of 0.5 are due to the shock cell structure found in the jet. They are the screech tones due to the phase locking of the radiated noise from the interaction of the large scale structures with the shock cell structure and the excitation of instability waves at the nozzle lip. These tones are most likely absent from the simulated jet due to its
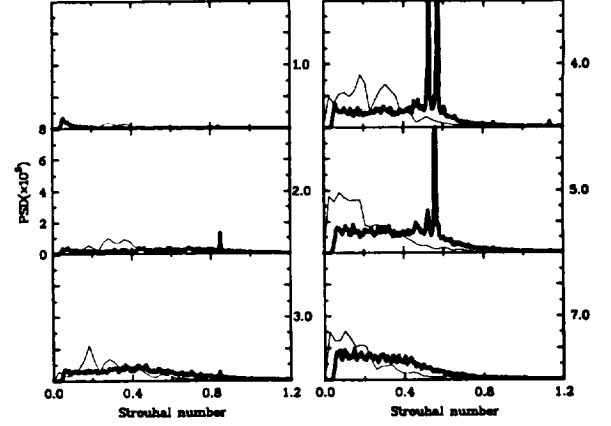

Figure 6: Power spectral density (PSD) of the mass flux in the at the maximum RMS location through the shear layer in the major axis plane for the varicose excitation. The numbers to the right of each spectra denotes the axial location. The heavy lines are the experimental results.
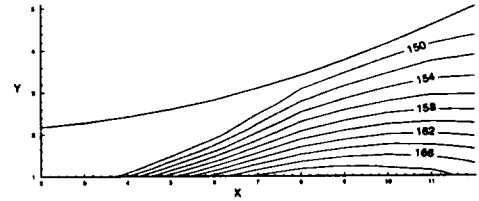

Figure 7: Near field sound pressure level (SPL) contours in the minor axis plane of the simulated jet excited by a varicose mode.

relatively weak shock cell structure.

In figure 7 sound pressure level (SPL) contours are shown in the minor axis plane of the simulated jet excited by a varicose mode. The definition of an SPL used here, consistent with Kinzie,[16] is :

$$SPL = 20 \log_{10}[\frac{P_{rms}}{P_{ref}}]$$ (18)

where

$$P_{ref} = [\frac{P_{ch}}{P_{atm}}](20 \times 10^{-6}) \ \frac{N}{m^2}$$ (19)

The pressure in the anechoic chamber, P_{ch}, during his experiments was 3080 N/m^2. The atmospheric pressure, P_{atm}, is 1.01325 × 10^5 N/m^2. The root mean square of the pressure, P_{rms}, is determined in the same manner as the data used for the hot wire comparisons. Consistent with the experimental data,[16] the noise appears to be generated at the end of the potential core and is directed in the downstream direction.

The remainder of this section will present and discuss far field noise predictions. For the far field noise predictions presented here the Kirchhoff surface is placed as

7

close to the jet as possible without intersecting regions of the jet plume where there are significant hydrodynamic fluctuations. Close proximity to the jet is desirable since the grid resolution is the finest there. Also, the closer the surface is to the jet, the less the pressure waves have to travel before reaching the surface. Thus, the numerical damping and dispersion errors are minimized. It is important not to place the surface too close to the jet since the Kirchhoff formula may interpret some hydrodynamic fluctuations as radiating ones.

The entire Kirchhoff surface is defined by four surface segments. Two surfaces are in the (i, j) plane and two are in the (i, k) plane (i is the axial index). The two end planes (perpendicular to the jet axis) are omitted. Since the noise propagation is predominantly in the downstream direction, the downstream end plane should not make any contributions to the noise levels at the observer locations used here (described below).

The grid used in the present study (shown in figure 2) is highly clustered near the nozzle lip region. This stretching varies in the axial direction so that a constant j or k grid line gradually moves away from the jet axis. This is very convenient in terms of deciding how to define the Kirchhoff surface. Each of the four surface segments can be placed very near the nozzle lip line at the nozzle exit plane. As the jet develops in the axial direction, and the mixing increases, the surface will gradually move away from the jet axis so that it never does intersect high mixing regions.

The Kirchhoff surface is illustrated in figure 8. The extent of the surface in the axial direction is from $x = 1D_{eq}$ to $20D_{eq}$. The surface is not extended to the wall so that the possibility of any effects it may have on the acoustic solution is reduced. The surface terminates at 20 diameters to reduce the effects of any reflections that may occur from the downstream boundary. The range of the domain covers the axial region where turbulent mixing noise is known to be generated, i.e., the region near the end of the potential core.

The lateral locations of the surface were determined by considering the mass flux perturbation levels. Figure 9 shows contours of the RMS of such perturbations in the major axis plane of the jet excited by a varicose mode. The grid (showing every tenth i grid line) is overlaid on the figures. The arrows (between $x = 11D_{eq}$ and $12D_{eq}$) point to the grid lines that seem to be optimal for the planes of the Kirchhoff surfaces perpendicular to each figure. It is apparent that the surfaces do not intersect any region where significant fluctuations are found. These appear to be the optimal locations and are used for the calculations. Similar reasoning is used in the minor axis plane. In a study of the sensitivity of the noise predictions to the location of the Kirchhoff surface, Lyrintzis[19] found that there is little difference between the results if the surface is placed at least one diameter away from the jet axis.
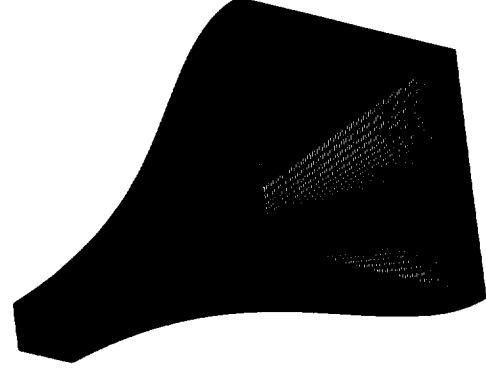

Figure 8: The surface used to for the far field (Kirchhoff) calculations.
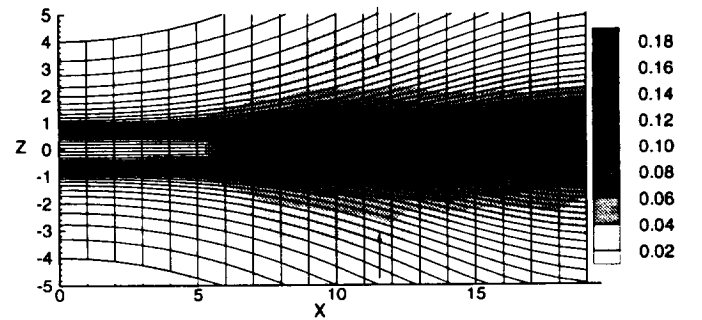

Figure 9: RMS of the mass flux perturbations in the major axis plane for the jet excited by a varicose mode. The values are normalized by the jet exit mass flux.
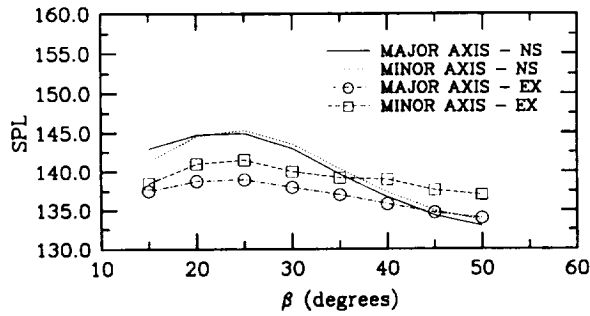
8

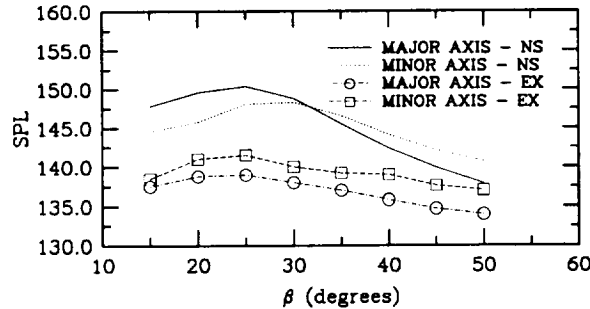Figure 10: Far field SPL levels for the varicose excitation.

Figure 11: Far field SPL levels for the flapping excitation.

The observer locations are selected to match the microphone stations used by Kinzie.[16] They consist of locations on an arc $25D_{eq}$ away from the center of the nozzle exit. The angular range is 15 to 50 degrees measured from the jet axis. Overall sound pressure levels in the far field are presented in figures 10 and 11 for the varicose and flapping excitation cases and compared to the experimental data. The figures are a function of the angle the observer makes with the jet axis and are commonly referred to as directivity plots.

For the locations close to the jet axis (i.e., small angle β), the simulation overpredicts the experimental data for both the varicose and flapping cases. This is most likely due the higher amplitude instability waves (coherent structures) found in the simulated jet. Recall that the simulation predicts a peak instability wave amplitude that is approximately twice that of the experimental jet. If the peak amplitude in the experimental jet is scaled by a factor of two, and one assumes that the noise is dominated by turbulent mixing noise, then the radiated pressure amplitude should be scaled by a factor of four (as deduced from the acoustic analogy[38]). This results in a twelve decibel increase in the radiated noise. If the noise is dominated by Mach wave emission, then the instability wave analysis[39] predicts that the radiated pressure be scaled by a factor of two, which results in a 6 decibel increase in the far field noise. The peak differences between the simulation and experiment for

the varicose and flapping excited jets are 7 and 12 dB, respectively. These differences suggest that the flapping jet has weak Mach wave radiation while the varicose jet noise is dominated by Mach wave radiation.

The good correlation between the discrepancy in the noise source prediction and the discrepancy in the far field noise prediction leads one to conclude that the algorithm is capable of predicting the far field noise radiation for a given source amplitude. This argument is strengthened by the good agreement in the trends of the simulated and the experimental jets. Considering first the comparison for the jet excited by a varicose mode (figure 10), the angle of peak noise radiation is correctly predicted to be near 25 degrees. The noise is more directional in the simulated jet, however, compared to the experimental one. Recall from the introduction that turbulent mixing noise is fairly directional. The shock cell structure in the experimental jet may explain why its noise is less directional. This structure leads to the additional shock associated noise generation mechanisms. Since this type of noise has upstream propagating components, it will tend to make the noise less directional when the contributions of all of the noise sources are combined. Although there is also a shock cell structure in the simulated jet excited by a varicose mode, it is comparatively weak.

The spectra of the far field noise in the major axis plane is shown in figure 12 for the simulated jet excited by a varicose mode. Like the hot wire spectra presented earlier, screech tones are apparent in the experimental data. Ignoring these tones, however, like the experimental jet, the simulated one does predict a fairly broad spectral peak centered near a Strouhal number of 0.2.

5 Conclusions

In this paper a general algorithm for the prediction of supersonic jet noise is presented. The algorithm consists of the numerical simulation of the noise sources and sound radiation to the acoustic near field. The time dependent near field solution is then passed on to a Kirchhoff formulation to determine the far field noise. The algorithm has been applied to a perfectly expanded, cold, supersonic rectangular jet problem. This geometry and set of flow conditions provide two advantages. The first is that turbulent mixing should be the sole noise generation mechanism present. This type of noise is found in the lower frequencies of the spectrum and therefore reduced the grid resolution requirements. The second advantage is that these conditions correspond to those of an experiment that has been conducted recently at Penn State. Thus, a comparison with the experimental data has been possible. This comparison has revealed that the algorithm is capable of reproducing
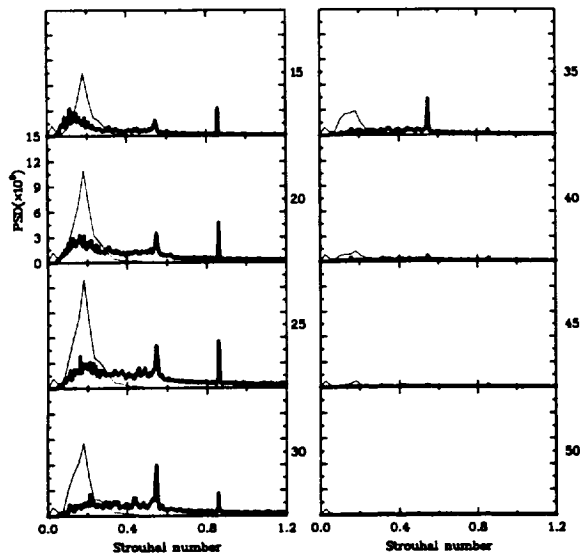
Figure 12: Far field noise spectra in the major axis plane for the flapping excitation. The numbers to the right of each graph denotes angular location in degrees. The heavy lines are the experimental spectra.

many of the flow and noise features found in the experimental jet. One discrepancy is that the simulation overpredicts the amplitude of the instability waves by a factor of two. Thus, future work on this project should investigate the reasons for this discrepancy and devise methods to eliminate it.

References

[1] Noise Standards for Aircraft Type Certification (Modifications to FAR Part 36). U.S. Environmental Protection Agency, Washington D.C., EPA 550/9-76-013, 197, 1994.

[2] Mankbadi, R. R., Hixon, R., Shih, S. H., and Povinelli, L. A. On the use of linearized Euler equations in the prediction of jet noise. AIAA Paper 95-0505, 1993.

[3] Viswanathan, K., and Sankar, L. N. Toward the direct calcuation of noise: fluid/acoustic coupled

simulation. *AIAA Journal*, **33**, pp. 2271-2279, 1995.

[4] Freund, J. B., Lele, S. K., and Moin, P. Matching of near/far-field equation sets for direct computations of aerodynamic sound. AIAA Paper 93-4326, 1993.

[5] Colonius, T., Lele, S. K., and Moin, P. Direct computation of the sound generated by a two-dimensional shear layer. AIAA Paper 93-4328, 1993.

[6] Mollo-Christensen, E. Jet noise and shear flow instability seen from an experimenters viewpoint. *American Society of Mechanical Engineers Journal of Applied Mechanics.*, **89**, pp. 1-7, 1967.

[7] McLaughlin, D. K., Morrison, G. L., and Troutt, T. R. Experiments on the instability waves in a supersonic jet and their acoustic radiation. *Journal of Fluid Mechanics*, **69**, pp. 73-95, 1975.

[8] Hussain, F., and Husain, H. S. Elliptic jets. Part 1. Characteristics of unexcited and excited jets. *Journal of Fluid Mechanics*, **208**, pp. 257-320, 1989.

[9] Grinstein, F. F. Vorticity dynamics in spatially-developing rectangular jets. AIAA Paper 93-3286, 1993.

[10] Rice, E. J., and Raman, G. Enhanced mixing of a rectangular supersonic jet by natural and induce screech. AIAA Paper 93-3263, 1993.

[11] Grinstein, F. F., Gutmark, E., and Parr, T. Numerical and experimental study of the near field of subsonic, free square jets. AIAA Paper 94-0660, 1994.

[12] King, C. J., Krothapalli, A., and Strykowski, P. J. Streamwise vorticity generation in supersonic jets with minimal thrust loss. AIAA Paper 94-0661, 1994.

[13] Zaman, K. B. M. Q. Effect of 'delta tabs' on mixing and axis switching in jets from asymmetric nozzles. AIAA Paper 94-0186, 1994.

[14] Quinn, W. R. Turbulent mixing in a low-aspect-ratio rectangular jet. AIAA Paper 95-2148, 1995.

[15] Zaman, K. B. M. Q. Axis switching and spreading of an asymmetric jet – role of vorticity dynamics. AIAA Paper 95-0889, 1995.

[16] Kinzie, K. W. *Aeroacoustic properties of moderate Reynolds number elliptic and rectangular supersonic jets.* Ph.D. thesis, Pennsylvania State University, 1995.

[17] Chyczewski, T. S. *A time-dependent, three-dimensional numerical study of supersonic rectangular jet flow and noise using the full Navier Stokes equations*. Ph.D. thesis, Pennsylvania State University, 1996.

[18] Farassat, F., and Myers, M. K. Extension of Kirchhoff's formula for radiation from moving surfaces. *Journal of Sound and Vibration*, **123**, pp. 451–460, 1988.

[19] Lyrintzis, A. S., and Mankbadi, R. R. On the prediction of the far-field jet noise using Kirchhoff's formulation. AIAA Paper 95-0508, 1995.

[20] Freund, J. B., Lele, S. K., and Moin, P. Calculation of the radiated sound field using an open Kirchhoff surface. CEAS/AIAA Paper 95-061, 1995.

[21] Hoffmann, K. A. *Computational fluid dynamics for engineers*. Engineering Education System, Austin, TX, 1989.

[22] Bayliss, A., and Turkel, E. Far field boundary conditions for compressible flow. *Journal of Computational Physics*, **48**, pp. 182–199, 1982.

[23] Tam, C. K. W., and Webb, J. C. Dispersion-relation-preserving finite difference schemes for computational acoustics. *Journal of Computational Physics*, **107**, pp. 262–281, 1993.

[24] Giles, M. B. Nonreflecting boundary conditions for Euler equation calculations. *AIAA Journal*, **28**, pp. 2050–2058, 1990.

[25] Colonius, T., Lele, S., and Moin, P. Boundary conditions for direct computation of aerodynamic sound generation. *AIAA Journal*, **31**, pp. 1574–1582, 1993.

[26] Thompson, K. W. Time-dependent boundary conditions for hyperbolic systems. *Journal of Computational Physics*, **68**, pp. 1–24, 1987.

[27] Thompson, K. W. Time-dependent boundary conditions for hyperbolic systems, II. *Journal of Computational Physics*, **89**, pp. 439–461, 1990.

[28] McLaughlin, D. K., Morrison, G. L., and Troutt, T. R. Reynolds number dependence in supersonic jet noise. *AIAA Journal*, **15**, pp. 526–532, 1977.

[29] Troutt, T. R. *Measurements on the flow and acoustic properties of a moderate Reynolds number supersonic jet*. Ph.D. thesis, Oklahoma State University, 1978.

[30] Morrison, G. L., and McLaughlin, D. K. Noise generated by instabilities in low Reynolds number supersonic jets. *Journal of Sound and Vibration*, **65**, pp. 177–191, 1979.

[31] Tam, C. K. W. The shock-cell structures and screech tone frequencies of rectangular and non-axisymmetric supersonic jets. *Journal of Sound and Vibration*, **121**, pp. 135–147, 1988.

[32] Troutt, T. R., and McLaughlin, D, K. Experiments on the flow and acoustic properties of a moderate Reynolds number supersonic jet. *Journal of Fluid Mechanics*, **116**, pp. 123–156, 1982.

[33] Özyörük, Y., and Long, L. N. A new efficient algorithm for computational aeroacoustics on parallel processors. *AIAA Journal*, **125**, pp. 135–149, 1996.

[34] Chyczewski, T. S., and Long, L. N. Applications of an efficient parallel computational aeroacoustics algorithm. CEAS/AIAA Paper 95-011, 1995.

[35] Jameson, A., Schmidt, W., and Turkel, E. Numerical solutions of the Euler equations by finite volume methods using Runge-Kutta time-stepping schemes. AIAA Paper 81-1259, 1981.

[36] Berman, C., Gordon, G., Karniadakis, G., and Orszag, S. Jet turbulence noise computations. AIAA Paper 93-4365, 1993.

[37] Bendat, J. S., and Piersol, A. *Random Data Analysis and Measurment Procedures*. John Wiley and Sons, New York, NY, 1986.

[38] Lighthill, M. J. Jet noise. *AIAA Journal*, **1**, pp. 1507–1517, 1963.

[39] Tam, C. K. W., and Burton, D. E. Sound generated by instability waves of supersonic flows. Part 2. Axisymmetric jets. *Journal of Fluid Mechanics*, **138**, pp. 273–295, 1984.